

Eulerian-Lagrangian Analysis of Cloud Evolution using CFD Coupled with a Sediment Tracking Algorithm

Sebastian Thomas* Vinod K. Lakshminarayan† Tarandeep S. Kalra‡ James D. Baeder§

The two-phase flowfield environment around a hovering micro-rotor is simulated using a fluid dynamics solver coupled with a Lagrangian sediment tracking algorithm. The present work attempts to examine the capabilities of a high fidelity CFD analysis together with a sediment tracking algorithm to analyze the evolution of brownout clouds. The effect of particle size on the evolution of the cloud and the predominant transport mechanisms are analyzed and compared with experimental data. The resolution of vortices for longer wake ages by the CFD solver along with better estimation of velocity profiles further outboard of the rotor were shown to be vital for the coupled simulation to achieve qualitative agreement with experiment. This better resolution is achieved through the use of additional overset meshes placed near the ground. Three size ranges of spherical particles are used to represent the sediment bed. The variation of the phenomenological attributes of the cloud evolution as a function of particle size was analyzed and found to agree with experimental evidence.

Nomenclature

a	Speed of sound, m s^{-1}
A	Rotor disk area, πR^2 , m^2
AR	Aspect Ratio, $AR = R/c$
c	Rotor chord, m
C_T	Rotor thrust coefficient, $T/(\rho A \Omega^2 R^2)$
C_{Toge}	Rotor thrust coefficient out of ground effect,
C_P	Rotor power coefficient, $P/(\rho A \Omega^3 R^3)$
C_{Poge}	Rotor power coefficient out of ground effect,
d_p	Particle diameter, μm
h	Height of rotor above ground, m
M	Mach number, V/a
r	Radial distance, m
z	Distance above ground plane, m
R	Rotor radius, m
V	Velocity, m s^{-1}
ρ	Flow density, kg m^{-3}
ρ_p	Particle density, kg m^{-3}
ψ	Wake age, degrees
Ω	Rotational frequency, Hz

Introduction

The brownout problem consists of the creation of a dense dust cloud that envelops the rotorcraft during in-ground effect operation. Apart from the obvious problem of rendering the pilot visually disoriented, these clouds can also be responsible for effects such as blade erosion and mechanical wear. Most of the current approaches to solving the brownout problem involve the use of improved sensor technology to increase pilot awareness or the employment of operational tactics such as specialized landing trajectories to avoid getting into a dangerous brownout situation. Although these solutions help in reducing the number of accidents due to brownout, it is still desirable to find a more permanent solution to this problem. Since the interaction of the rotor wake with the ground and the dust particles form the root cause of the brownout problem, it is believed that a detailed understanding of the underlying fluid physics coupled with a knowledge of the fluid-particle interaction under these conditions can help in the development of effective means of preventing and/or mitigating the adverse effects of rotorcraft brownout.

In recent years, significant progress has been made on experimental analysis of the brownout problem in the laboratory in a controlled environment. The main experimental difficulty comes in simulating the various brownout conditions, particularly with a full-scale rotor. To overcome the problem arising due to scale, experiments were performed at the University of Maryland to study the effect of the proximity to ground (Ref. 1) and the phenomenon of particle entrainment (Refs. 2, 3) on a hovering MAV-scale rotor. It is believed that a large amount of insight of the actual brownout phenomenon can be obtained through stud-

* Graduate Research Assistant, <sthomas2@umd.edu>

† Research Associate, <vinodk1@umd.edu>

‡ Graduate Research Assistant, <tkalra@umd.edu>

§ Associate Professor, <baeder@umd.edu>

ies conducted at this smaller scale. Detailed particle image velocimetry (PIV) measurements of the flowfield were performed by Lee et al. (Ref. 1) and showed a whole host of phenomena such as diffusion, vortex stretching and turbulence generation occurring close to the ground. Also, vortex pairing was seen to be an important mechanism by which stronger velocities were induced near the ground. PIV measurements were used by Johnson et al. (Ref. 2) to study the entrainment and upliftment of sediment particles. The development of the wall jet at the ground plane was observed to be key in the process by which the sediment particles reach their threshold velocities for lift off from the ground. Recently, Sydney et al. (Ref. 3) used PIV and flow visualization techniques to understand the various transport and uplift mechanisms taking place as the brownout cloud evolves around the same hovering micro-rotor. Sydney et al. observed and identified six different transport mechanisms that take place in the particle phase:

1. Creep - particles just slowly move along the sediment bed
2. Modified saltation bombardment - uplifted particles fall back to the ground and upon impact release additional particles from the sediment bed
3. Vortex trapping - uplifted particles are entrained into, and circle, individual vortices
4. Unsteady pressure effects - particles are uplifted in a direction perpendicular to the direction of jet flow due to a pressure gradient between the sediment bed and the vortex core
5. Reingestion bombardment - uplifted particles are accelerated around a vortex and then fall back to the ground causing the release of more particles from the sediment bed
6. Secondary suspension - particles are kept in suspension by being transferred from one vortex to the next

While experimental analysis is of immense importance in the understanding of the underlying physics of the brownout problem, it can be very difficult and time consuming to conduct a whole array of parametric studies in the laboratory. In comparison to the experiments, computational analysis can easily simulate a wide range of brownout conditions.

Brownout is an example of two-phase flow, where the fluid and the entrained particles interact with each other causing the transfer of momentum from one phase to the other. Any modeling of the phenomenon, therefore, requires the coupling of a fluid dynamics solver with a sediment tracking algorithm. Most of the present research concerning brownout assumes a one-way interaction between

the two phases i.e the particles are influenced by the flow-field but the fluid is unaffected by the particles. This is a reasonable first approximation for dilute flows and the present work makes use of this assumption.

Over the last few years, researchers modeling brownout have employed aerodynamic models of various levels of sophistication. Syal et al. (Refs. 4, 5) and Wachspres et al. (Ref. 6) performed computational analysis of full-scale rotorcraft brownout clouds using a sediment tracking algorithm coupled with a time-accurate, free-vortex method (FVM) with an image plane to simulate the ground. FVM is a very efficient numerical scheme for the preservation of far-wake vortical structures. The main disadvantage of the free-wake method is that it needs empirical models to approximate the ground boundary layer. In addition, FVM, without a fast summation algorithm, is an $O(n^2)$ method, implying that the run-time increases to large levels when the wake discretization is increased. This problem has been largely circumvented through the use of parallelization and fast multipole algorithms along with GPU computing. In Ref. 7, an inviscid vorticity transport model (VTM) was coupled with a particulate transport model to generate brownout clouds. Though, the tip vortex is better represented by using VTM as compared to FVM, even this methodology requires the approximation of the ground boundary layer. Wenren et al (Ref. 8) used a vorticity confinement method to better resolve the tip vortex. However, vorticity confinement methods use empirical factors that may not be easily determined in ground plane simulations.

Recently, Kalra et al. (Ref. 10) used a high-fidelity compressible Reynolds Averaged Navier Stokes (RANS) solver to simulate the hovering micro-rotor setup of Lee et al., described earlier. The primary objective of this study was to demonstrate the capability of RANS to provide good flow-field predictions for a hovering rotor operating close to the ground. The results were validated by comparison of predicted integrated thrust and power measurements with experimental data. The tip-vortex trajectory predicted by the RANS simulation compared well with experiment. Though this methodology is relatively very expensive, unlike in the case of FVM or VTM, no boundary layer approximation is needed in this case. The aerodynamic model captures the boundary layer without the need for empiricism. However this work did not perform a full brownout simulation.

The current work extends the analysis of Kalra et al. to perform full brownout simulation using one-way coupling between the CFD solution and the particle code. This work aims to demonstrate the capability of using a RANS based flow solver with a reliable sediment code for particle transport to predict various transport mechanisms observed in the experiments of Sydney et al. (Ref. 3). The sediment code chosen to couple with the CFD solution is the same algorithm used by Syal et al. in Refs. 4, 5. In

Ref. 5, this solver was validated by comparison of simulated, full-scale cloud geometries with photogrammetry measurements from experiment. Furthermore, based on the work by Greeley et al (Ref. 9), Syal et al. (Ref. 5) have introduced the effect of unsteady pressure effects on the mobility of the sediment particles.

In the work of Kalra et al. (Ref. 10), even though the mesh was well refined to resolve tip vortex evolution and its interaction with the ground, they did not preserve the vortices to sufficient distance in the radial direction, and therefore may not capture some or all of the brownout phenomenon. This work initially presents the improvements in flowfield predictions by using a refined mesh, which captures the tip vortex till further outboard locations. This is then followed by a detailed visualization of particle transport close to the ground using three different particle sizes. Finally, the overall brownout clouds from the original mesh system (used by Kalra et al.) and the refined mesh systems are compared to see if better resolution of vortices in the far-field contributes substantially to the way in which the brownout cloud evolves in the simulations.

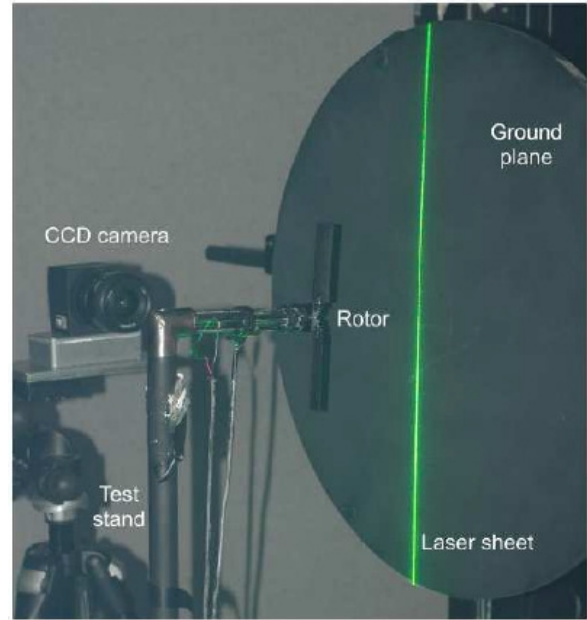
Rotor Configuration

As mentioned before, the micro-hovering rotor studied in Refs. 1-3 is simulated in this study. The flow visualization results from Lee et al. (Ref. 1) are used to validate the aerodynamic solver and the results from Sydney et al. (Ref. 3) are used to validate the particle transport mechanisms predicted in the current simulation. The experimental setups of Lee et al. and Sydney et al. are shown in Fig.1.

The experiments were done on a 2-bladed hovering rotor. The blades are rectangular and untwisted with an aspect ratio of 4.39. The blades have a circular arc airfoil with 3.7% thickness and 3.3% camber. The rotor was operated at a constant collective pitch of twelve degrees. The experimental results were obtained at a root Reynolds number of 6,480, a tip Reynolds number of 32,400 and a tip Mach Number (M_{tip}) of 0.08. The experiments were conducted at rotor heights varying from 0.25R to 1.5R. In the current study, the focus will only be on the 1R rotor height case.

Methodology

Accurate modeling of the brownout cloud evolution around the micro-rotor requires the employment of a coupling strategy wherein data is exchanged between the computational flowfield and the sediment tracking algorithm. Since the blade is assumed to be perfectly rigid, there is no need to include a structural solver in the coupling framework. For the purposes of the paper, the following models are used:



(a) Experimental setup of Lee et al.



(b) Experimental setup of Sydney et al.

Fig. 1. Experimental setups

Flow Dynamics Solver

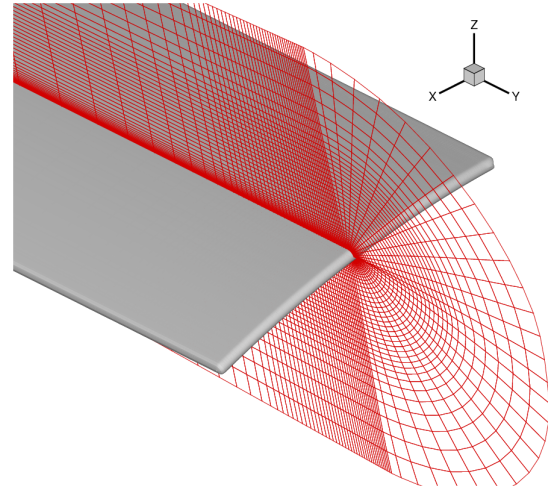
Fluid dynamics computations are performed using a RANS based solver OVERTURNS (Ref. 11). The simulations are done in a time-accurate manner in an inertial frame of reference. The code solves the compressible RANS equations using a preconditioned dual-time scheme in the di-

agonalized approximate factorization framework (Refs. 12, 13). The diagonal form of the implicit approximate factorization method was originally developed by Pulliam and Chaussee (Ref. 14). Low Mach preconditioning (Ref. 15) is used not only to improve convergence but also to improve the accuracy of the solution. The inviscid terms are computed using a third order MUSCL scheme (Ref. 16) utilizing Korens limiter (Ref. 17) with Roe's flux difference splitting (Ref. 18) and the viscous terms are computed using second order central differencing. The Spalart-Allmaras (Ref. 19) turbulence model is employed for the RANS closure. This one-equation model has the advantages of ease of implementation, computational efficiency and numerical stability. The production term in this eddy-viscosity model is modified (Ref. 20) to account for the reduction in turbulence levels at the vortex core due to rotational effects.

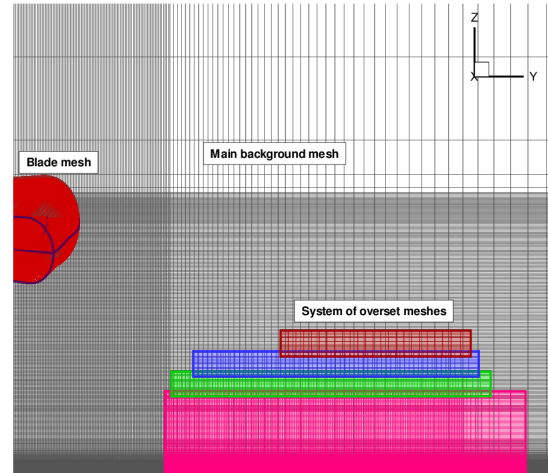
Mesh System

Two separate mesh systems were used to understand the importance of resolving the far-field vortices in brownout simulations. The first was the grid system employed by Kalra et al. (Ref. 10) which consisted of a body conforming blade mesh and a single background mesh. The main background mesh was refined to accurately resolve tip vortices all the way to the ground. The mesh was further refined near the ground to resolve the boundary layer.

In this work, in an attempt to better resolve vortices of older wake ages, a system of overset cylindrical meshes is embedded into the main background mesh, as shown in Fig.2. The overset meshes are laid down in a stair-step manner with the most refined overset mesh placed at the bottom and the coarsest mesh at the top. This strategy is adopted to limit the cell size disparity between various overset meshes to less than a factor of two in the regions of interpolation, and therefore, minimize the errors arising due to these interpolations. Using stair step type meshes allows the mesh cell size to slowly increase from the well refined region near the ground to a coarse outboard region. Implicit hole-cutting technique, developed by Lee (Ref. 21) and improved by Lakshminarayan (Ref. 11), is used to determine the connectivity between the overset meshes. Table 1 shows the number of points used by the various meshes. The most refined overset mesh (overset mesh 1) is placed near the ground and the coarsest mesh (overset mesh 4) is placed at the top. In order to reduce the computational cost, the flow is assumed periodic in the azimuthal direction. This allows the 2-bladed rotor to be simulated using one half of the computational domain. The main as well as the overset background meshes have 187 points in the azimuthal direction, with a grid plane placed every 1° of the azimuth. The total number of grid points in the refined overset mesh system is 20.1 million points and this constitutes a 75% in-



(a) Body fitted C-O mesh



(b) Refined grid system used in the RANS simulations

Fig. 2. Mesh system used in the RANS simulation of the micro-rotor

Mesh	Dimensions	Mesh points (in millions)
Blade Mesh	267x93x50	1.2
Main Background Mesh	187x230x304	13.1
Overset Mesh 1 ^x	187x186x146	5.1
Overset Mesh 2 ^x	187x111x20	0.4
Overset Mesh 3 ^x	187x61x20	0.2
Overset Mesh 4 ^x	187x25x20	0.09

^xOnly part of refined mesh system

Table 1. Number of points used in the various meshes

crease in the number of points compared to the unrefined mesh system.

Sediment Tracking Algorithm

The particle tracking algorithm used in this work is developed in Refs. 4, 5. It consists of a Lagrangian method with empirical models for the various phenomena involved in sediment transport. Entrainment of particles into the flowfield is modeled using the Bagnold-like model (Ref. 22). Bombardment is modeled using the Hu and Shao model (Ref. 23). The particles are assumed to be perfect spheres and the drag force acting on the particle is an empirical function of Reynolds number. The particles are convected using a third order backward difference time-stepping scheme. Particle collisions and unsteady pressure effects are ignored. The solver has demonstrated the capability of simulating millions of sand particles in a GPU environment aided with clustering techniques. Timestep convergence of particle trajectories is obtained for the particle properties, flow environment and numerical algorithms employed in the current analysis at a rotational discretization of 1 degree or less, as shown in Fig. 3 for a single particle trajectory for three levels of discretization.

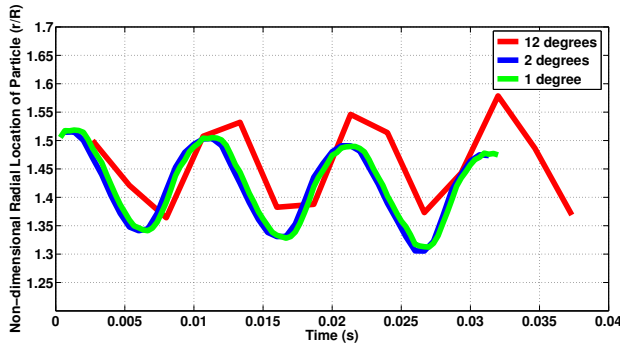


Fig. 3. Variation in the radial location of a particle with time for three different levels of time discretization

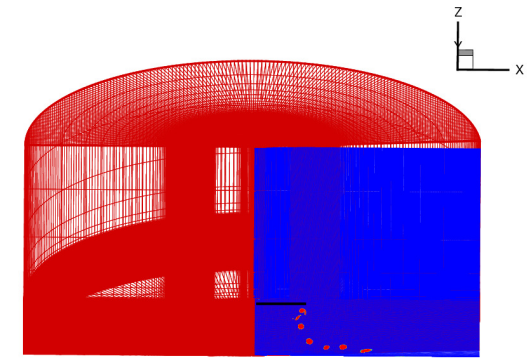
Coupling Strategy

As mentioned before, the coupling of the CFD solution to the particle transport is done using one-way coupling, such that the particles do not influence the evolution of the flowfield. This approach allows the CFD simulation to be done independent of the sediment code. A single snapshot of CFD solution, rotated with time, is used for this analysis.

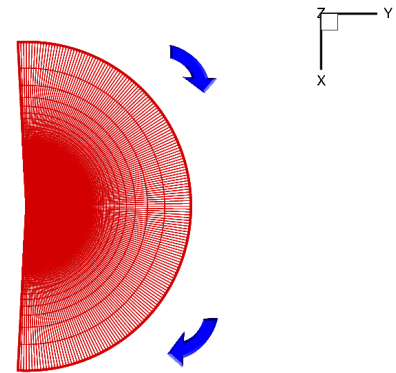
The RANS simulation using both the original and the refined mesh system is performed using a time step size of 0.25 degrees of rotation of the blade. The simulation is done for 20 revolutions to obtain flowfield convergence. Each iteration of the flow-solver uses six sub-iterations to remove linearization error. The time taken for each simulation is 6 days using 32 processors for the original mesh system and

the same number of days using 72 processors for the refined mesh system.

To couple the flowfield with the sediment code, the solution is saved every 12 degrees azimuth from the last revolution, giving thirty snapshots of flow solution to approximate the unsteady flow-field. To compute the velocity at a particular azimuthal plane, the solution data sets that bound that plane, can be rotated to that particular azimuth before performing a weighted average to get an approximation for the flowfield at this plane. In the present work, in order to couple the flowfield with the sediment code, a single three dimensional snapshot of the flowfield is rotated and the location of the particle with respect to the CFD grid was computed using three binary searches along the three orthogonal axes. The velocity at the particle location is found through a simple tri-linear interpolation of the velocities at the vertices of the grid that contain it. Figure 4 illustrates this idea. This method of approximating the flowfield is not as com-



(a) Three-dimensional snapshot of the solution



(b) Rotation of the solution to simulate the flowfield (as seen from below)

Fig. 4. Strategy used to couple RANS with sediment tracking algorithm

putationally intensive as the alternative approach of tightly coupling RANS with the sediment tracking algorithm and running them serially. This is because the sediment cloud can take as many as 50 revolutions before it is fully matured

	C_T/C_{Toge}	C_P/C_{Poge}
RANS	1.15	1.06
Experiment	1.17	1.05

Table 2. Thrust and power comparison with experiment for a rotor height of 1.0R

and the runtime for the RANS computations will become prohibitively large. The advantage of using a single snapshot is that the CFD simulation can be performed prior to computing the sediment trajectories. In addition to reducing computational time, this approach requires minimal memory requirements since we are saving only one solution as opposed to several solutions per revolution.

Results and Discussion

The results section is divided into two parts. The first part is concerned with the validation and analysis of the micro-rotor aerodynamic flowfield predicted by the CFD simulations. The second part describes the analysis of the physics behind particle upliftment in this aerodynamic environment. Since the particle code used in the current simulations is developed by Syal et al. (Ref. 4), no detailed validation of this methodology is performed as a part of this work. Instead, the methodology is directly used to simulate the brownout cloud.

Aerodynamic Flowfield Simulation

Validation of the Fluid Dynamics Solver All computations are done for rotor height of 1R above the ground. Table 2 shows the comparison of integrated performance obtained using the refined mesh system with the measured experimental data for this rotor height. Shown are the IGE to OGE thrust and power ratios. One can clearly see a good agreement between CFD and experimental data. It should be noted that the OGE thrust and power predicted by the experiments were 0.0133 and 0.00227, respectively, while that predicted by CFD is 0.0143 and 0.00249, respectively. The difference is possibly due to the difficulty in setting the exact collective in experiment. Note that the performance obtained using the original mesh system is comparable to the current results.

The validation of the flowfield is done by comparing phase-averaged azimuthal vorticity contours at three different wake-ages (0° , 60° and 120°) shown in Fig. 5. The plot also shows the velocity vectors. For the purpose of clarity, the vectors are plotted only one in every four points in the normal direction and one in every four points in the radial direction from the mesh used for simulation. From the plot, it can be seen that the predicted wake trajectory is very similar to that of the experiments at all wake-ages for both the refined as well as the original mesh system.

The tip vortices are initially observed to contract under the effect of the rotor wake. However, as they approach the ground the vortices begin to move radially outward. In the process, the filaments elongate and the vortex core initially begins to reintensify. Eventually, the vortices start to become less stable, with an increase in wandering, and hence the development of aperiodicity. At these later wake ages the tip vortices predicted by the original mesh system seem to convect more rapidly in the radial direction as compared to the predictions from the refined mesh system or the experimental measurements. Furthermore, the introduction of the additional overset meshes closer to the ground captures the aperiodicity in the flowfield as well as the increase in tip vortex wandering seen in the experiments. As a result, the vortices at older wake ages get smeared out during phase-averaging of the refined mesh solution, and the predicted vorticity contour levels are closer to the experimentally measured levels. Significant wake instabilities are not captured in the RANS simulations using the original mesh system and hence, the phase-averaging does not smear out the vorticity magnitude.

Though, the phase-averaged results show smeared out vortices at later wake ages, an instantaneous snapshot of the vorticity contours at zero degree wake age (shown in Fig. 6) reveals that the simulations with the refined mesh system are able to capture tip vortices of older wake ages compared to the original mesh system. Also, note from this plot that the tip vortex is still significantly strong even after 4 blade passages due to the intensification caused by the stretching of the vortex filament.

A more detailed validation of the CFD methodology is done by looking at the variation of radial velocity as a function of height at various radial locations, shown in Fig. 7. It is clear that for inboard locations, both the original mesh system as well as the refined mesh system predict velocity profiles that match well with the experiment. However, at outboard sections, where the results from using the original mesh system does not show good agreement with the experimental data, the results from the use of the refined mesh systems shows an improved prediction. The height of the wall jet is seen to decrease as one moves radially outward. As a consequence, there is initially an increase in the peak radial velocities at larger radial distance. At $r/R = 2.0$ it is observed that the peak radial velocity finally begins to decrease. Overall the use of the refined mesh system is clearly seen to improve the flowfield prediction, such that there is better agreement with the experimental data as compared to the original mesh prediction.

Predicted Global Vortical Structure The overall vortical structure of the flowfield can be best visualized by plotting an iso-surface of q -criterion (Ref. 24) colored by vorticity contours. Figure 8 compares the instantaneous computa-

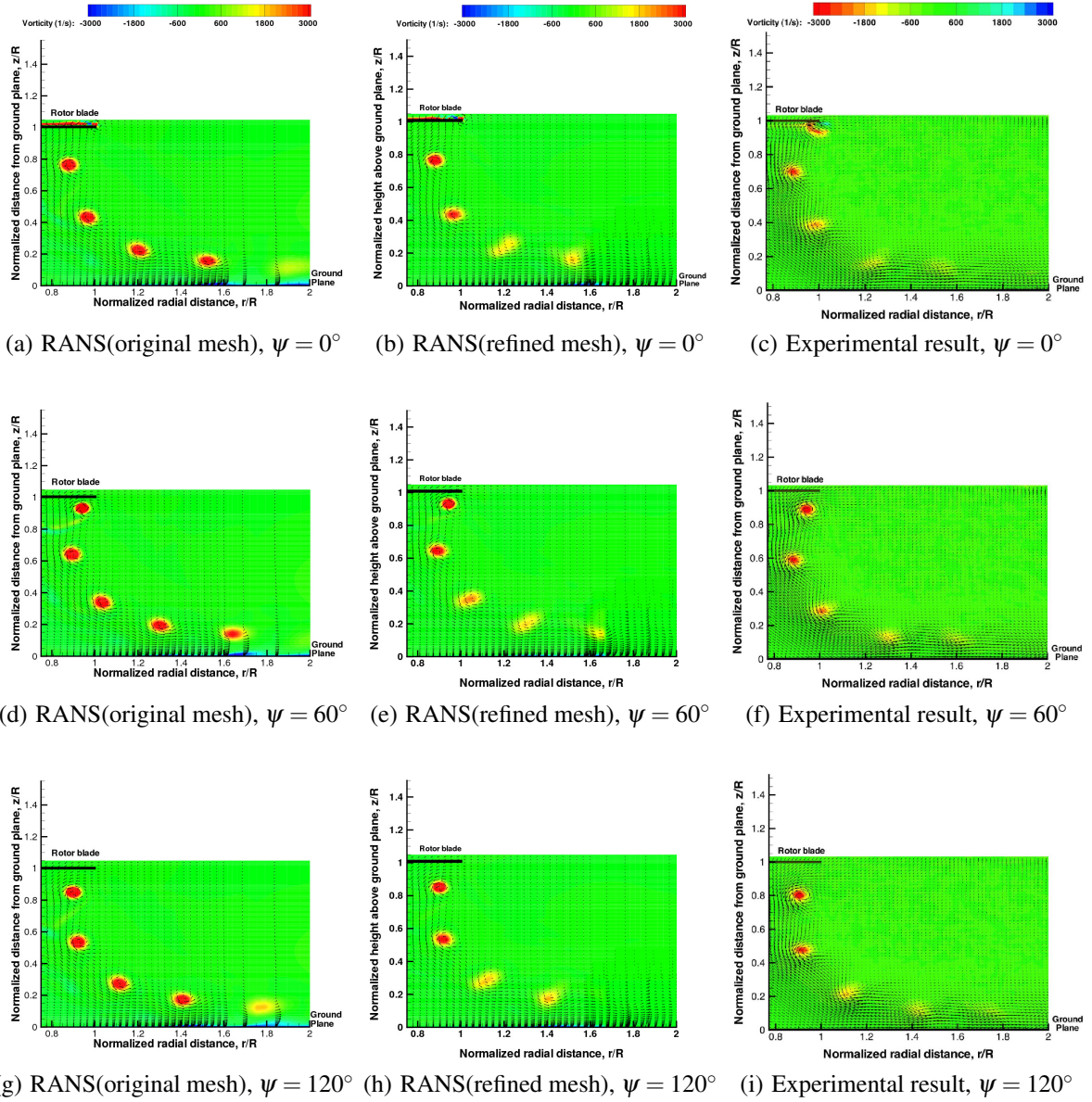
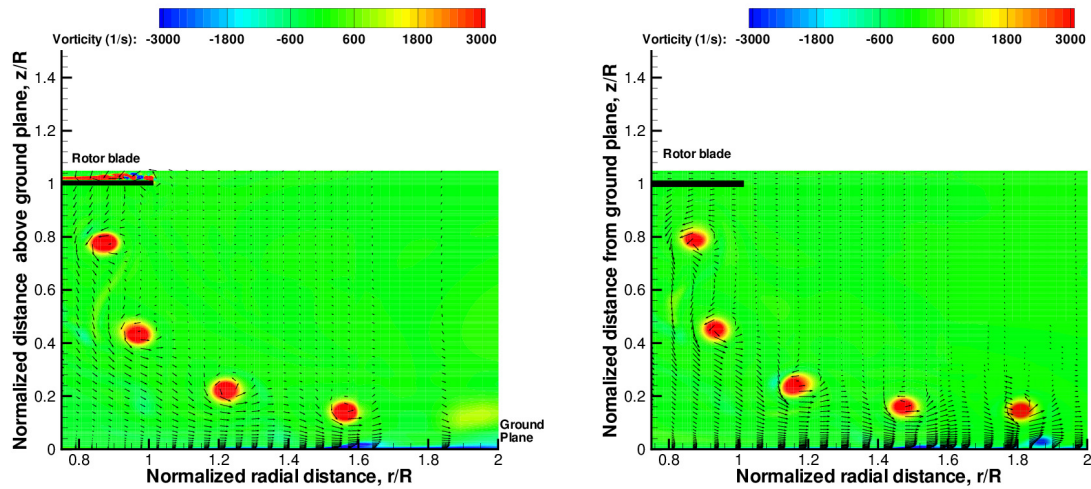


Fig. 5. Comparison of CFD predicted phase-averaged vorticity contours with experimental data for a rotor height of $h/R = 1.0$

tional predictions of the three-dimensional structure of the tip-vortex trajectory using the two grid refinement levels. For clarity, the flowfield from entire domain is shown even though the simulation was done only using half the domain. It is clear that the RANS simulation with grid refinement is better able to resolve the tip-vortex for longer wake ages as well as capture the vortex instability near the ground. A quantitative estimate of the tip vortex wandering and instabilities can be obtained by looking at the wake trajectory. Figure 9 shows the radial and vertical positions of the tip vortices as a function of wake age for both the mesh systems. Clearly, while the trajectories from the two mesh sys-

tems are almost similar till the point the wake is resolved by the original mesh system, the trajectory from refined system shows development of instabilities at the later wake ages.

Predicted Aerodynamic Flow Physics near the Ground Plane To understand the details of the flow physics close to the ground, Fig. 10 shows the velocity vectors along with the pressure contours (normalized by freestream value) for the refined mesh system. For the purpose of clarity, the vectors are plotted only one in every four points in the normal direction and one in every eight points in the radial direction



(a) Instantaneous vorticity contours (original mesh) (b) Instantaneous vorticity contours (refined mesh)

Fig. 6. Instantaneous vorticity contours at $\psi = 0^\circ$

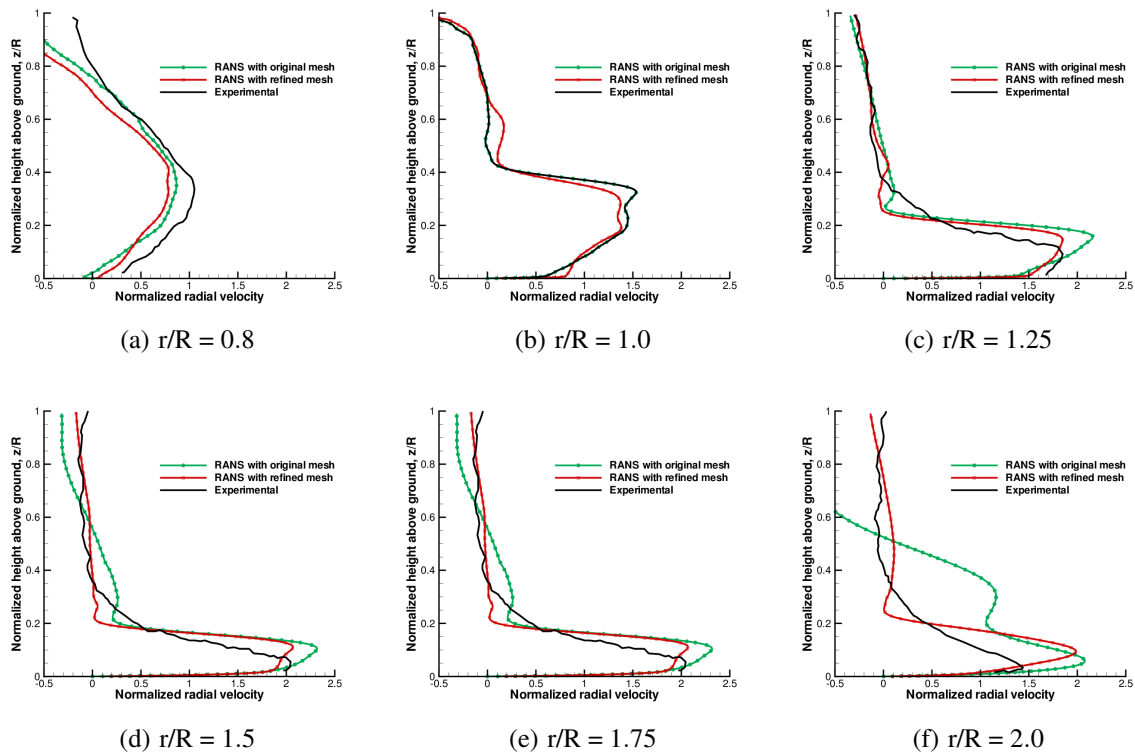


Fig. 7. Variation of radial velocity as a function of height at various radial locations

from the mesh used for simulation. Fig. 11 shows a close-up of the pressure contours near the ground plane. The vectors are plotted only one in every two points in the normal direction and one in every four points in the radial direction from the mesh used for simulation. The tip vortex can be easily

identified by the low pressure region. There is a region of high pressure on the ground corresponding to the stagnation location. The jet flow at the ground is directed outwards at locations outboard of the stagnation point and inwards inboard of it. The boundary layer developed near the ground

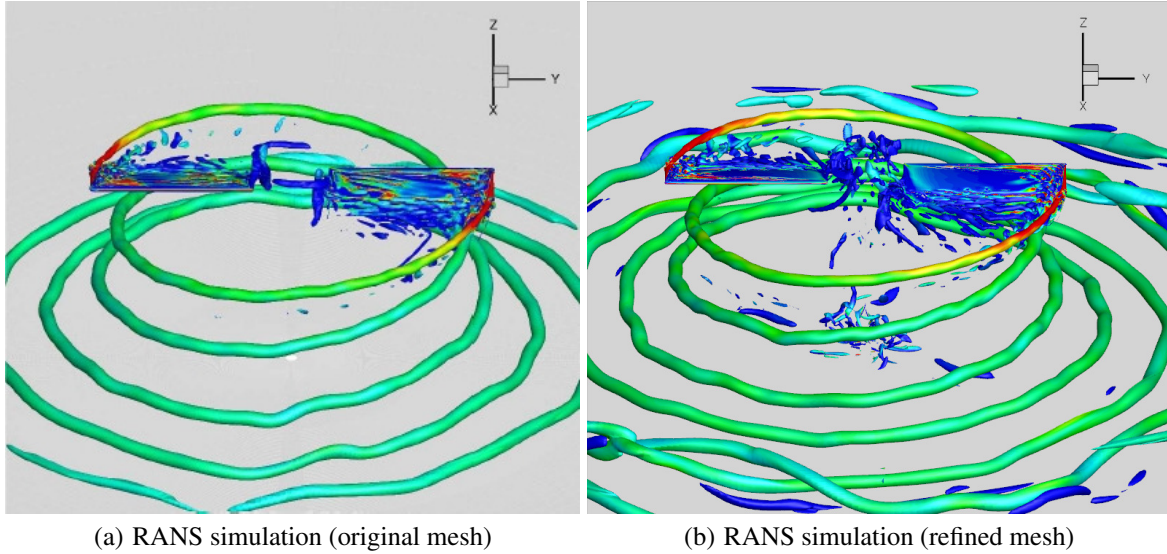


Fig. 8. Isocontours of q -criterion, $q=0.25$, colored by vorticity

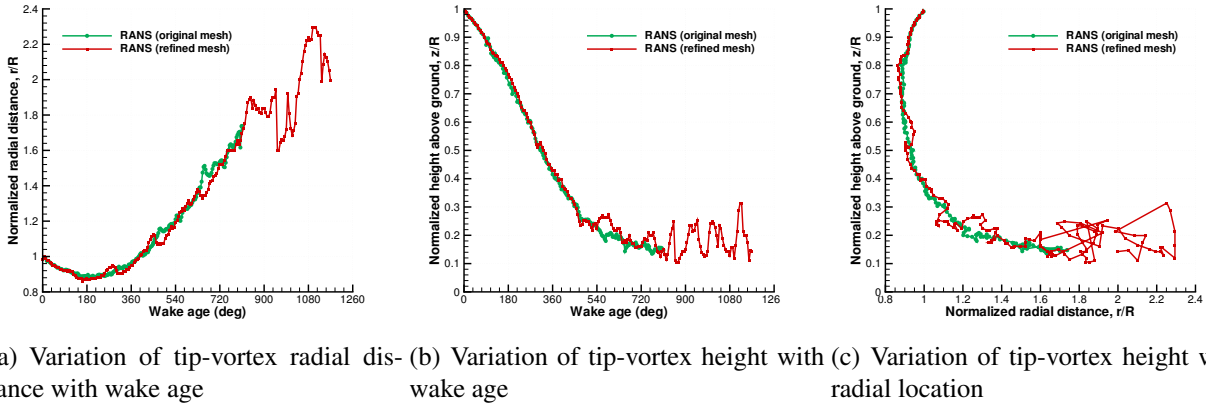


Fig. 9. Wake trajectory predictions using RANS

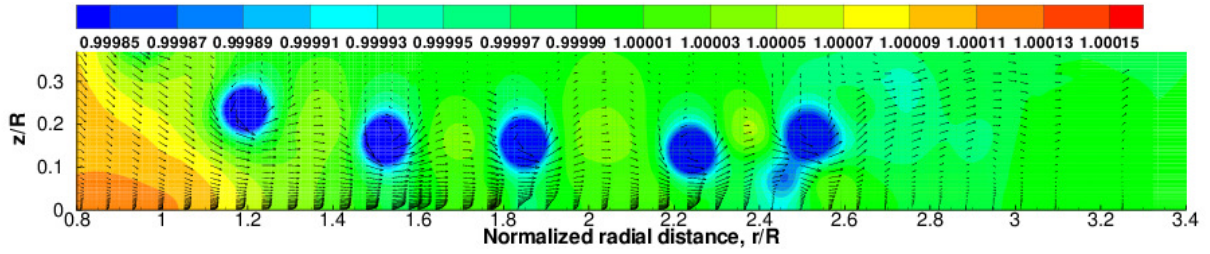
is mostly laminar, which becomes more turbulent at regions directly below the tip vortex as a result of additional local induced velocity. Figure 12 shows eddy viscosity contours at a wake age of 120 degrees. The region of higher eddy viscosity formed directly below the vortex can be seen, which corresponds to the turbulent boundary layer region observed in the velocity vector plots. The induced velocity from the tip vortices close to the ground causes the jet flow on the ground to separate and form a separation bubble. It is seen that the separation bubble formed at one wake-age peels off from the ground plane at a later wake-age forming an opposite sign vortex. The opposite sign vortex is then observed to further interact with the tip vortex.

Brownout Cloud Simulation

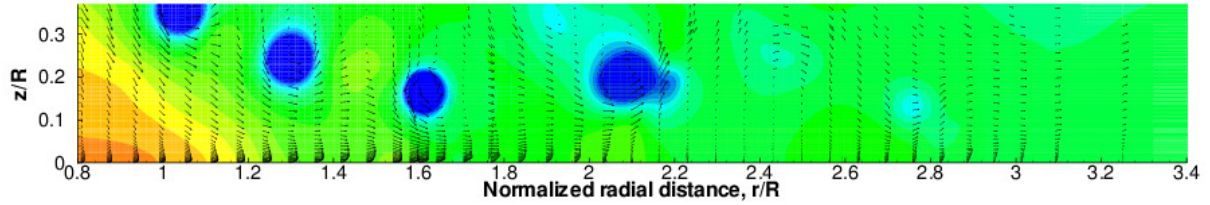
Having validated the accuracy of the CFD predicted aerodynamic flowfield, the brownout cloud is simulated using the obtained solutions from the original as well as refined mesh system.

Particle and Sediment Bed Characteristics To simulate the cloud, a square-shaped sediment bed of side equal to $6R$ was placed directly below the micro-rotor at a rotor-height of $1\%R$. The number of layers in the sediment bed was set to 200.

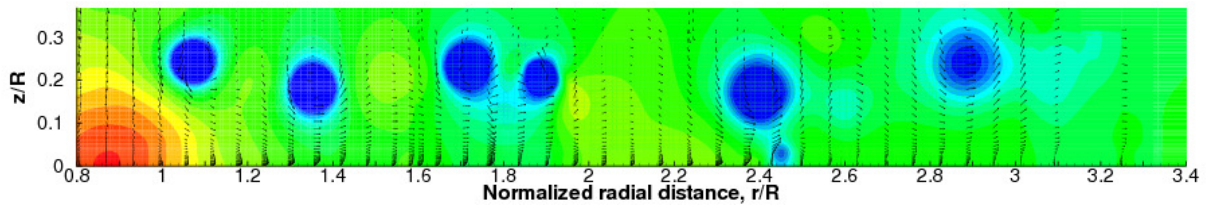
Three different particle sets were used in the simulations to mirror the experimental work conducted by Sydney et al. (Ref. 3). In Ref. 3, three different sets of spherical glass beads having density of $1300\text{kg}/\text{m}^3$, but varying



(a) Isocontours of pressure at $\psi = 0^\circ$



(b) Isocontours of pressure at $\psi = 60^\circ$



(c) Isocontours of pressure at $\psi = 120^\circ$

Fig. 10. Velocity vectors along with pressure (non-dimensionalized by freestream value) contours

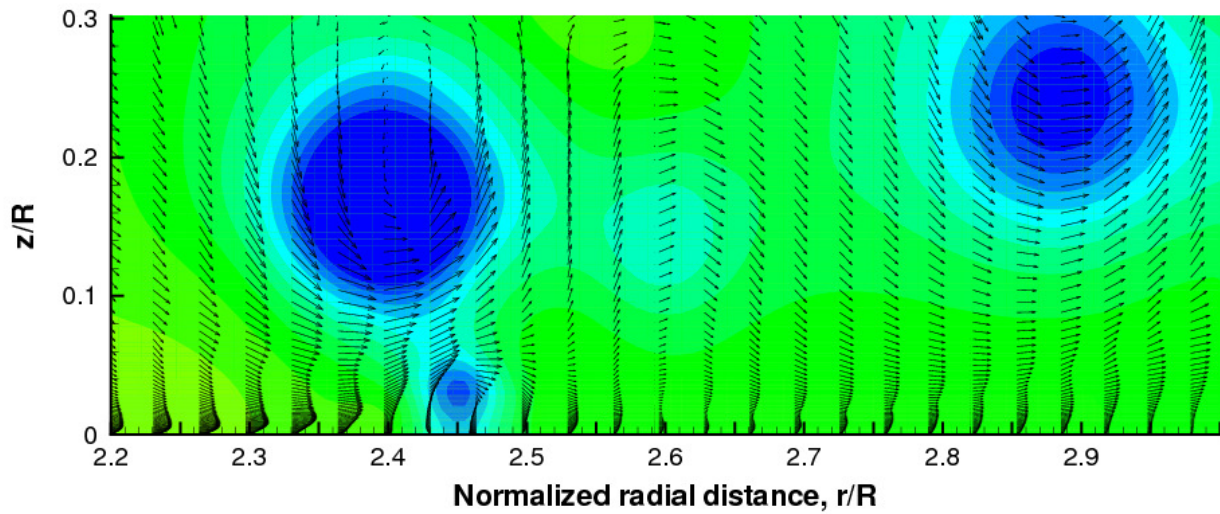


Fig. 11. A close-up of the pressure contours near the ground at $\psi = 120^\circ$

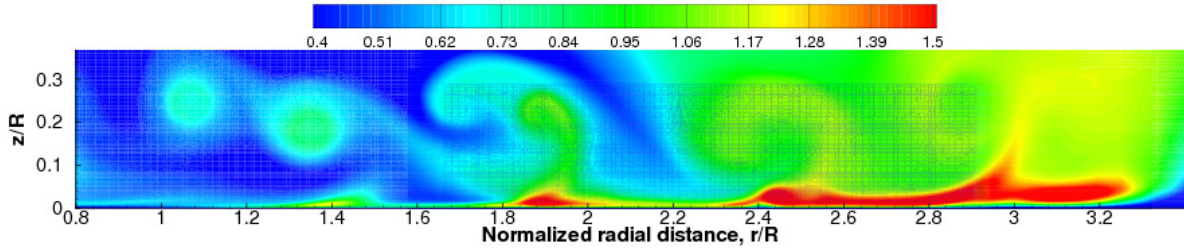


Fig. 12. Eddy viscosity contours at $\psi = 120^\circ$

in diameter were used to study the effect of particle size on the phenomenological attributes of the brownout cloud. For the simulations, particles with similar density as the experiment are used, however, the chosen particle sizes are different. The particle sizes from the experiment and the simulation are shown in Table 3. The reason for examining the different modeled particle sizes can be explained using Fig. 13. The figure shows the threshold friction velocity

Particle Set	Diameter (microns)	Expt. diameter (microns)
A (heavy)	50	100
B (intermediate)	1	50
C (light)	0.2	1

Table 3. List of particle parameters used in the coupled simulations

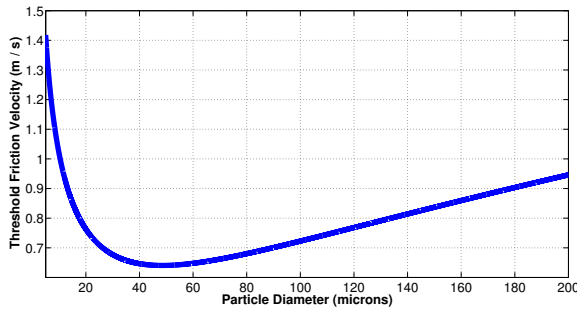


Fig. 13. Variation of threshold friction velocity with particle diameter

above the particle moves as a function of particle diameter. The threshold velocity is seen to be minimum for the intermediate-sized particles used in the experiment. The lighter particles have higher threshold velocity due to increased cohesion between the particles, while the larger particles are too heavy to be lifted off the ground. The curve shown in the plot can be shifted to the right or left by changing the parameters that model the particle cohesion. In the current simulations, the model was kept unchanged from what Syal et al. had used in their simulations in Refs. 4, 5. Therefore, to show the phenomenological effects of light, intermediate and heavy particles on the brownout cloud, appropriate particle sizes are chosen that are different from the experimentally used size (glass beads will have different cohesion than sand particles).

Brownout Cloud Evolution As described previously, the wake capturing methodology can be coupled to the sediment tracking algorithm by rotating, and interpolating be-

tween, thirty different snapshots of the flowfield over the course of one revolution. However, for the current work only a single snapshot is utilized. The local velocity at the particle location was found through the tri-linear interpolation of the vertex values of the grid cell that contains the particle. The following observations can be made regarding the particle transport using the three different particle sizes described above.

Particle Set A In simulations involving particle set A, it is observed that even though the sediment bed in this case became very mobile, none of the particles are ever uplifted into suspension. The particles simply creep along the ground plane in a direction that is predominantly radial. Figure 14 shows the creep mechanism exhibited by the heavy particles in set A. Sydney et al. (Ref. 3) reported similar observations in experiments with heavy glass spheres (see Fig.15). The heaviest particles were found to simply roll or hop along the surface and very few were uplifted into suspension.

Particle Set B In simulations involving particle set B, in addition to the phenomenon of creep, the phenomenon of saltation bombardment is observed. Saltation bombardment involves the temporary upliftment of a particle which then proceeds to follow a ballistic-like trajectory back to the ground plane potentially causing the ejection of more particles. In Ref. 3 saltation bombardment was described to be a cascading process that manifested in a significant increase in airborne particle density at increasingly downstream distances. The newly ejected particles from saltation bombardment were found to immediately creep or saltate unless they

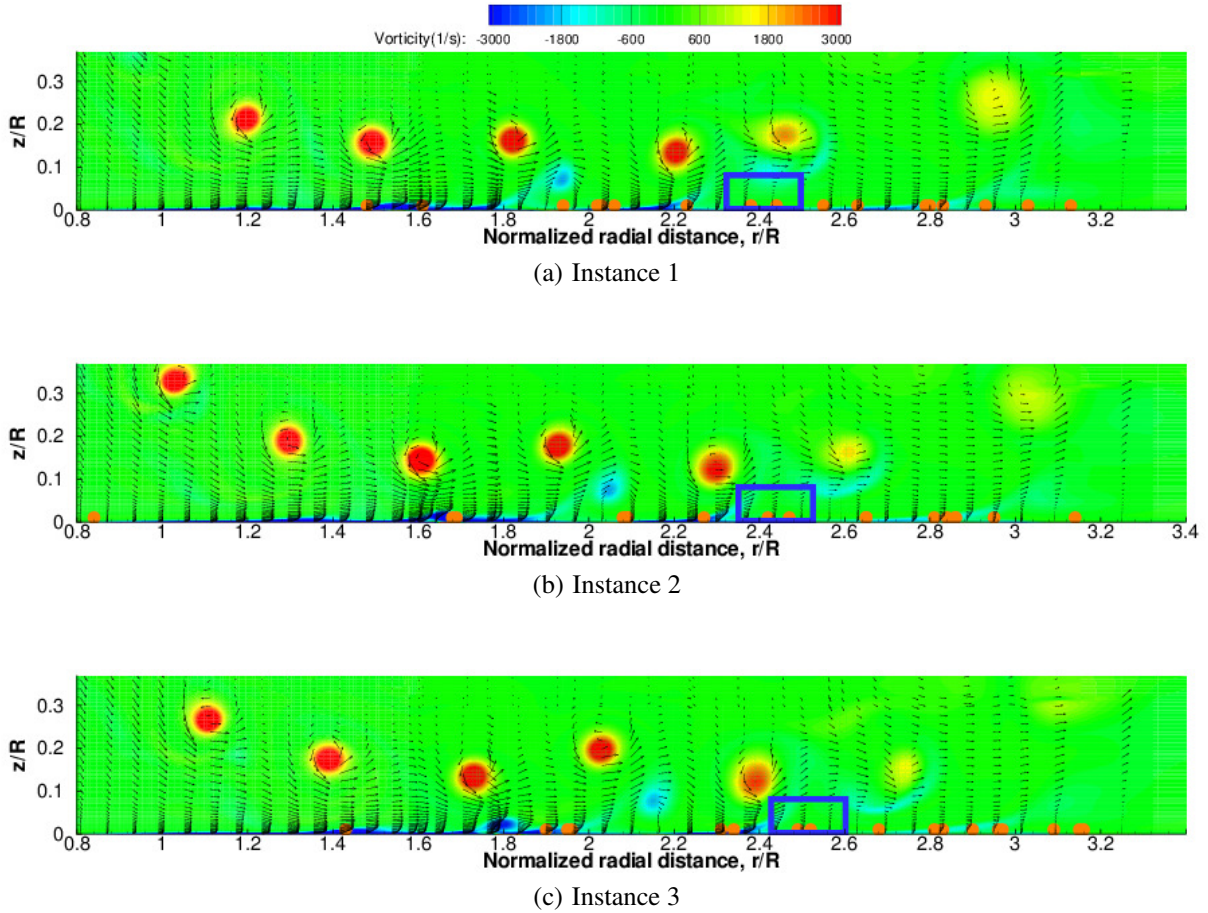


Fig. 14. The creep mechanism observed in simulations involving the 50 micron particles

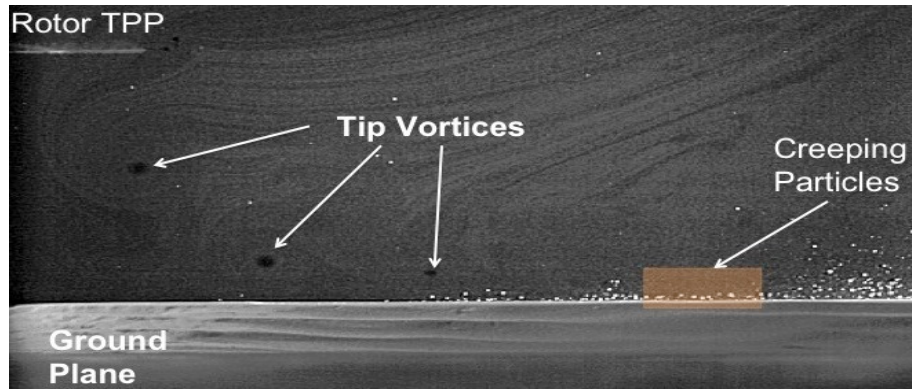


Fig. 15. The creep mechanism observed in experiments involving the intermediate particles (45-63 microns)

were directly entrained, leading to the ejection of even more particles from the bed.

In numerical simulations, saltation bombardment is observed almost all across the sediment bed including regions near the shaft. Figure 16 shows one example of the process. In a short span of time, a wavy active saltation layer

is found to develop and several particles are uplifted out of this layer by close proximity vortices. The mechanism of saltation bombardment seen in simulations is in very good qualitative agreement with experimental observations seen in Fig.17.

Another mechanism observed in the numerical experi-

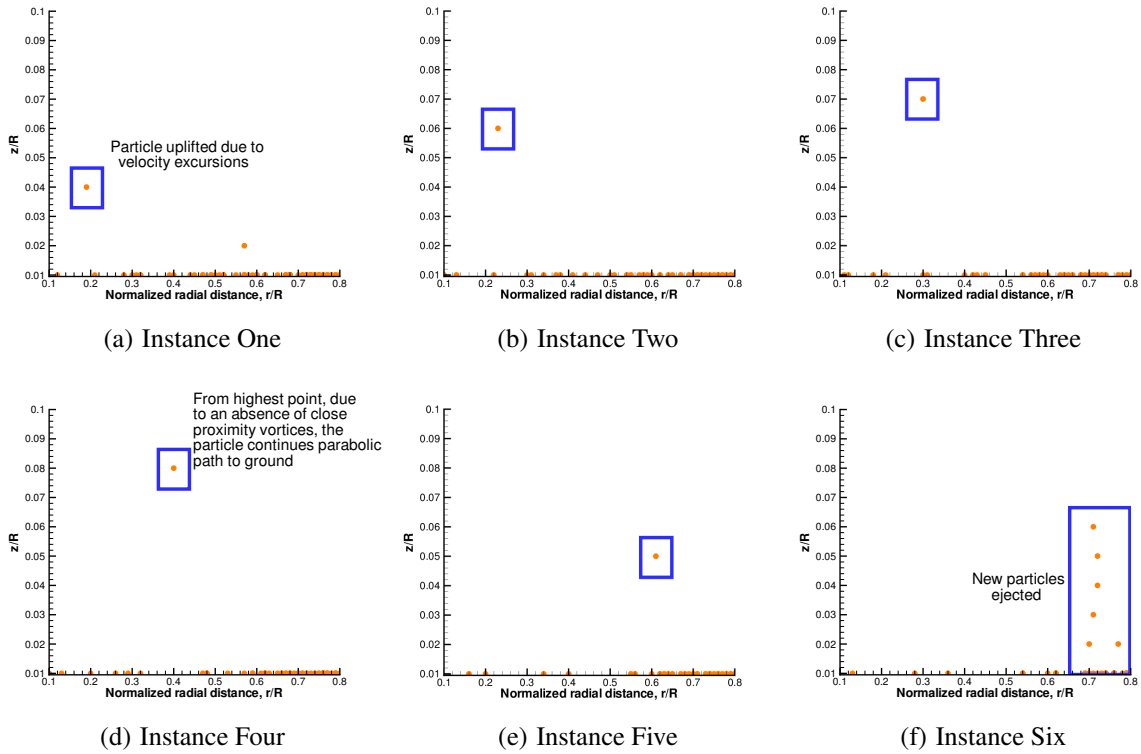


Fig. 16. The process of saltation bombardment observed in simulations close to the rotor shaft for a particle size of 1 micron

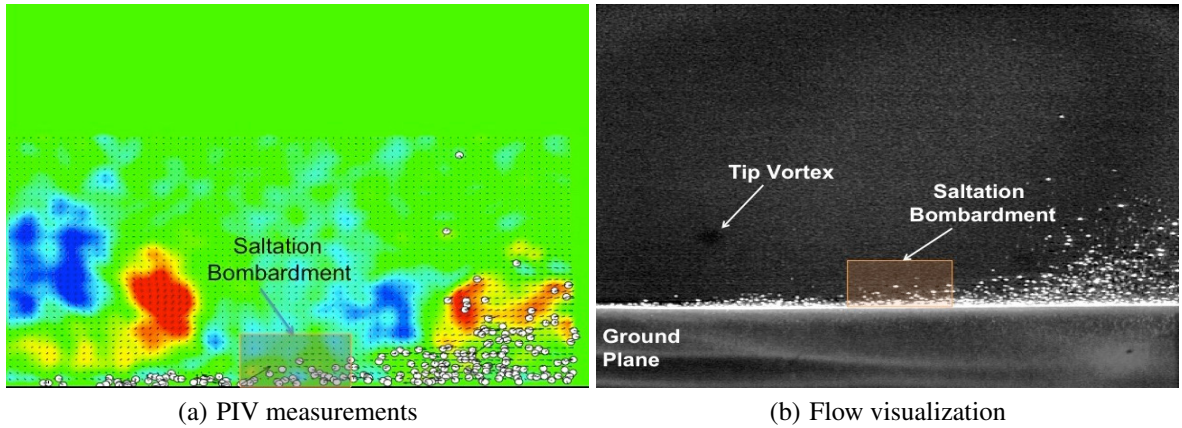


Fig. 17. The mechanism of saltation observed in experiments for a particle size of 50 microns

ments is vortex trapping. Particles are initially uplifted by vortices coming into close proximity with the ground. By the time the particles have reached a sufficient height off the ground plane, the original vortex has passed on or dissipated and the particles are then entrained into subsequent vortices. Figure 18 shows an example of the process that

is obtained in the numerical simulation. The mechanism of vortex trapping was reported by Sydney et al. (Ref. 3) to be one of the key mechanisms by which particles are lifted into suspension. Figure 19 shows PIV measurements and flow visualization for one instance of the vortex trapping phenomenon. The numerical simulations not only capture this

mechanism of particle transport, the results compare very well with the experimental data.

Figure 20 shows a snapshot of the particle distribution seen in the laboratory experiments conducted by Sydney et al. (Ref. 3). The sediment waves seen in experiment are also predicted by the numerical simulations as illustrated in Fig. 21.

Particle Set C The simulations involving particle set C show neither a mobile sediment bed nor any particles being uplifted into suspension. This is because the entrainment model used in the sediment tracking algorithm predicts a very high threshold friction velocity needed for the sub-micron particles in set C and this threshold exceeds the maximum velocity magnitude observed at the sediment ground plane. So even without a rigorous model for particle cohesion, the formulation of the entrainment model predicts that particles in set C will not be lifted up. This is illustrated in Fig.22 which is similar to Fig. 13, but zoomed in near the smaller particle size. These results are similar to the observations made in the experiments by Sydney et al. (Ref. 3) where the lightest particles were the least mobile due to strong cohesive forces between particles of small sizes.

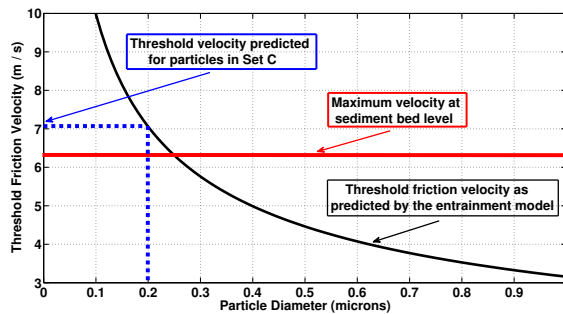


Fig. 22. Variation of threshold friction velocity with particle diameter

The Effect of Grid Refinement This section discusses the effect of improving the resolution of vortices of older wake ages on the phenomenological qualities of the brownout cloud. The sediment tracking algorithm is coupled with the solutions predicted by RANS using two different grid refinements discussed before. The particle characteristics chosen are those belonging to particle set B. Figure 23 illustrates the differences between the predictions of the cloud formation from the two RANS solutions. Without grid refinement, as seen in Fig.23(a), the vortices dissipate before reaching a radial distance of $2R$. Accordingly, the opposite-sense vorticity created at the wall in this region is proportionately reduced leading to a less energetic saltation layer.

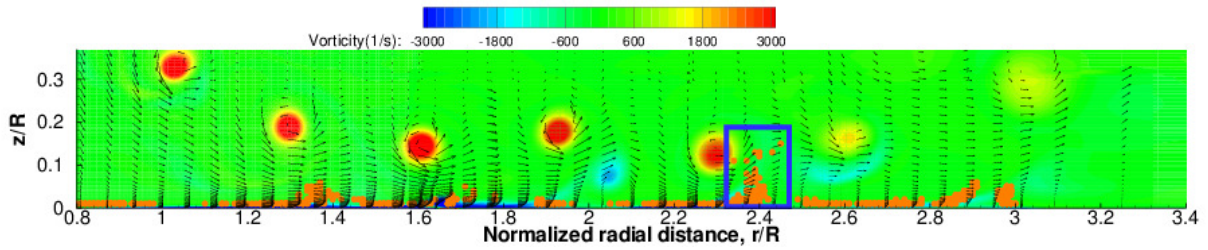
The lack of mobility in the saltation layer precludes the upliftment of particles through the mechanisms of saltation bombardment or vortex trapping.

Grid refinement substantially improves the mobility predictions in the sediment bed. Figure 23(b) shows the results using the refined mesh system in the RANS calculations. Due to the better resolution of the vortex at later wake ages, the regions of anti-vorticity near the ground are seen to be stronger. This in turn forces particles off the ground enabling them to be entrained into passing vortices. The formation of sediment waves is also predicted using the refined solution while there is no evidence of similar structures when the unrefined CFD solution is used in the coupling. This clearly indicates that in order to accurately capture various brownout phenomena, one needs to resolve the wake sufficiently far outboard.

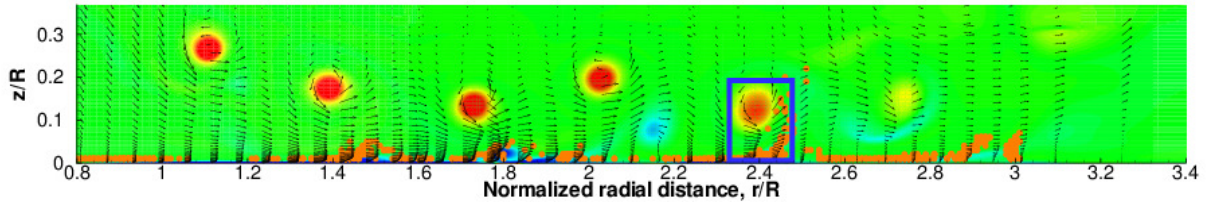
Summary and Conclusions

A high fidelity CFD model was coupled with a sediment tracking algorithm in order to simulate and form comparisons of brownout cloud development in the flowfield generated around a micro-rotor. Two different grid refinements were attempted to understand the effect of better resolved vortices in the far-wake on the evolution of the brownout cloud. A simulation of brownout cloud evolution around a micro-rotor was demonstrated by coupling the RANS flowfield with a sediment tracking algorithm. The simulations were conducted using three different particle diameters to understand the effect of particle size on the phenomenological attributes of the respective clouds. Listed below are the specific observations/conclusions.

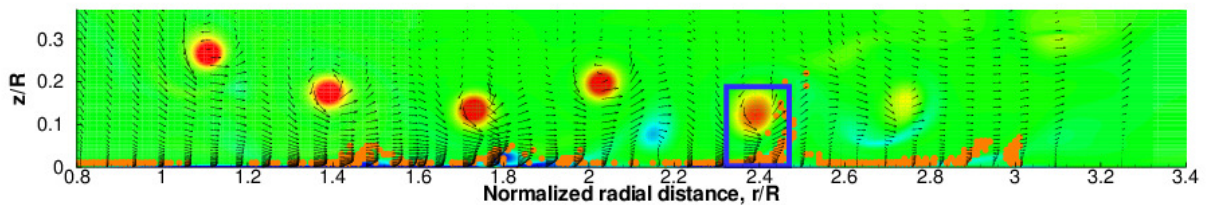
1. For a high-fidelity RANS solution for the flowfield beneath a micro-rotor hovering in ground-effect, a refined mesh system (as compared to the original mesh system used by Kalra et al. (Ref. 10)) was better able to resolve vortices of older wake age as well the regions of separated flow near the ground.
2. The phase averaged azimuthal vorticity contours for different wake ages showed good comparison with the experimental results in terms of wake trajectory. With the usage of the refined mesh system, the predicted strength of the vortices and their radial location, especially at later wake-ages, showed better correlation with the experimental data.
3. The comparison of predicted time-averaged radial velocity profiles with the experimental data at outboard radial locations showed considerable improvement with the use of the refined mesh system.
4. Flow visualization, with the aid of q -criterion, showed a larger amount of tip vortex instabilities for the refined mesh system solution as compared to that from



(a) Particles uplifted by passing vortex

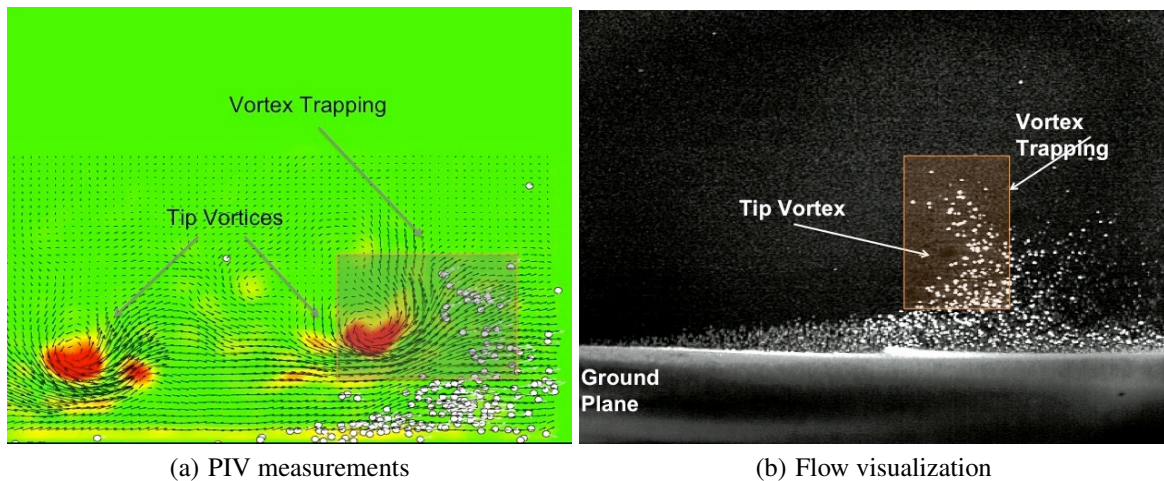


(b) Particles re-energised by second vortex



(c) Particles trapped by second vortex

Fig. 18. The vortex trapping mechanism observed in simulations for a particle size of 1 micron



(a) PIV measurements

(b) Flow visualization

Fig. 19. The vortex trapping mechanism observed in experiments for a particle size of 50 microns

the original mesh system solution used by Kalra et al. (Ref. 10)

5. Velocity vectors colored by the pressure contours at various wake ages showed the mechanism of separa-

tion induced by the proximity of tip vortices to the ground. Furthermore, the local induced velocity of the tip vortex closest to the ground caused the boundary layer to transition to a more turbulent state.

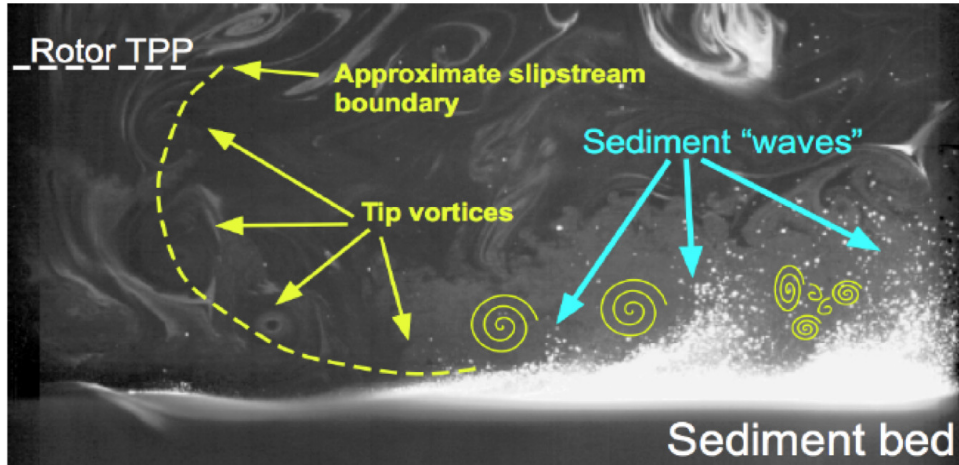


Fig. 20. Formation of sediment waves observed in experiments for a particle size of 50 microns

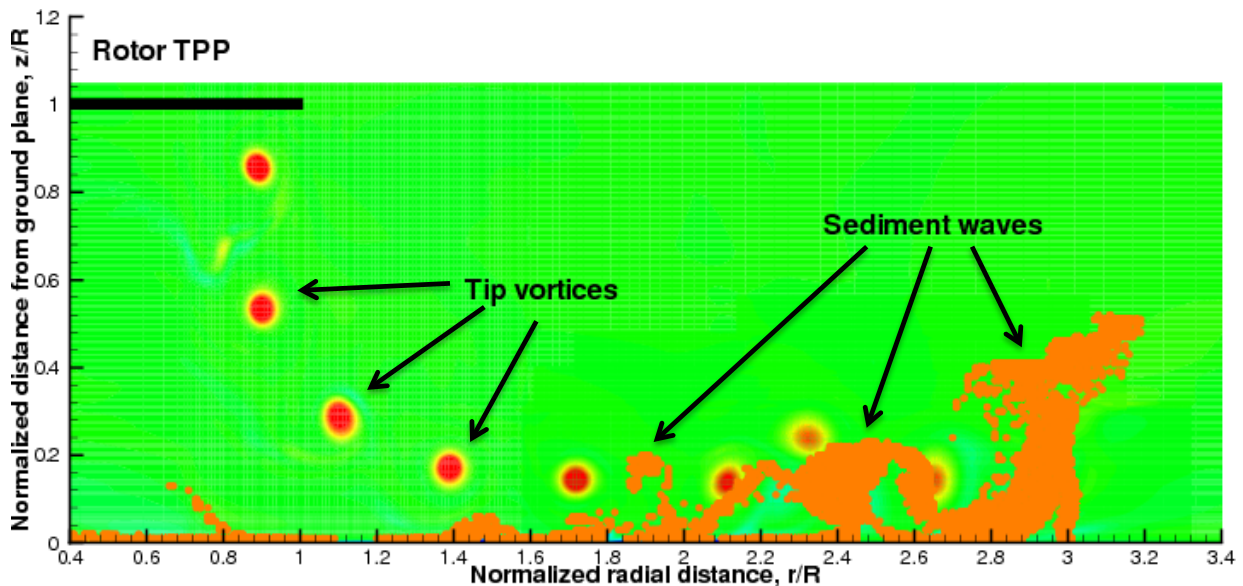
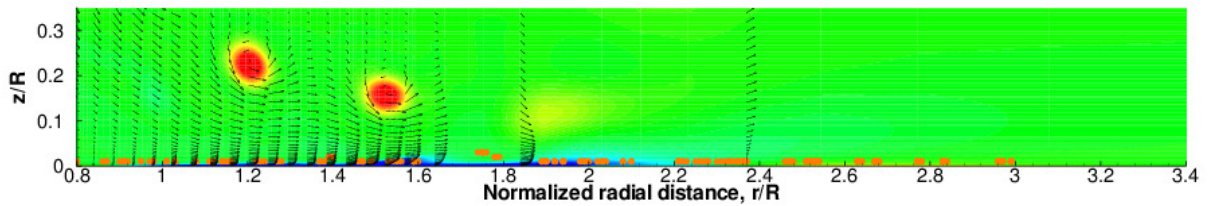
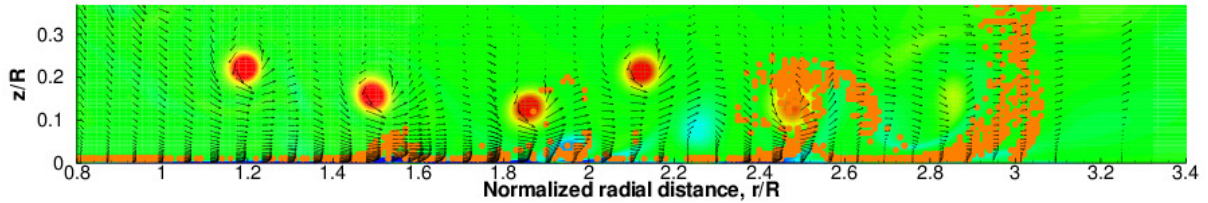


Fig. 21. Formation of sediment waves observed in simulations for a particle size of 1 micron

6. A plot of eddy viscosity contours further confirmed that most of the region near the ground is transitioning to turbulent flow. An increase in eddy viscosity was seen at locations on the ground directly below the vortex.
7. The brownout simulation showed that the heaviest particles (50 microns) crept along the ground plane without being uplifted into suspension.
8. The lightest particles (0.2 microns) experienced no motion whatsoever; a result similar to that reported in Ref. 3 wherein experiments with the lightest particles resulted in the least mobile bed due to cohesive forces between particles that dominate at this end of the size spectrum.
9. The intermediate sized particles (1 micron) were observed to be the most mobile under the given conditions, exhibiting most of the phenomena observed in laboratory experiments conducted by Sydney et al. (Ref. 3). The mechanisms of creep, saltation bombardment and vortex trapping were observed to occur during the simulation.
10. For the same particle dimensions, it was found that grid refinement in the RANS simulation yielded better phenomenological agreement with experimental results. This was due to the better resolution of vortices of older wake ages and, by extension, better modeling



(a) Sediment mobility predicted by the simulation using the original mesh system



(b) Sediment mobility predicted by the simulation using the refined mesh system

Fig. 23. The effect of grid refinement on the prediction of cloud evolution for a particle size of 1 micron

of the velocity distribution near the ground plane outboard of the rotor. While the RANS simulation with grid refinement predicted a very mobile bed for the 1 micron particles, the simulation with just a single background mesh predicted little to no upliftment.

Low pressure regions are associated with the vortex cores, therefore future work will incorporate the unsteady pressure effects on motion of the sediment particles by coupling the pressure field predicted by CFD with the sediment tracking algorithm. Furthermore, a more rigorous cohesion model needs to be utilized to analyze transport mechanisms that occur for glass sphere particle sizes in the sub-micron regime for a more quantitative comparison to experimental data. In addition, an increase in predicted aperiodicity is expected by including additional CFD snapshots of the flowfield in time over one revolution, rather than just one snapshot. Finally, once the predicted brownout cloud is quantitatively validated, CFD can be used to understand better the Reynolds number scaling effects and to assess the effects of rotor geometry on brownout cloud mitigation.

Acknowledgments

The Air Force Office of Scientific Research supported this work under a Multidisciplinary University Research Initiative, Grant W911NF0410176. The contract monitor was Dr. Douglas Smith. The authors would like to thank Anish Sydney and Ajay Baharani for providing PIV and flow visualization images from their experimental studies. The authors also wish to thank all of their colleagues at the University of Maryland, Government research labs, and the rotorcraft

industry for the valuable discussions on the brownout problem.

References

- ¹Lee, T. E., Leishman, J. G., and Ramasamy, M., "Fluid Dynamics of Interacting Blade Tip Vortices With a Ground Plane," *Journal of the American Helicopter Society*, Vol. 55, (2), April 2010.
- ²Johnson, B., Leishman, J. G., and Sydney, A., "Investigation of Sediment Entrainment in Brownout Using High-Speed Particle Image Velocimetry," Proceedings of the 65th Annual American Helicopter Society Forum, Grapevine, TX, May 27–29, 2009.
- ³Sydney, A., Baharani, A., and Leishman, J. G., "Understanding Brownout Using Near-Wall Dual-Phase Flow Measurements," Proceedings of the 67th Annual American Helicopter Society Forum, Virginia Beach, VA, May 3–5, 2011.
- ⁴Syal, M., Govindarajan, B., and Leishman, J. G., "Mesoscale Sediment Tracking Methodology to Analyze Brownout Cloud Developments," Proceedings of the 66th Annual American Helicopter Society Forum, Phoenix, AZ, May 11–14, 2010.
- ⁵Syal, M., and Leishman, J. G., "Comparisons of Predicted Brownout Dust Clouds with Photogrammetry Measurements," Proceedings of the 67th Annual American Helicopter Society Forum, Virginia Beach, VA, May 3–5, 2011.

- ⁶Wachspress, D.A., Whitehouse, G.R., Keller, J.D., Yu, K., Gilmore, P., Dorsett, M., McClure, K., "High Fidelity Rotor Aerodynamic Module for Real Time Rotorcraft Flight Simulation, Proceedings of the 65th Annual American Helicopter Society Forum, Grapevine, TX, May 27–29, 2009.
- ⁷Phillips, C., Kim, H., and Brown, R. E., "The Flow Physics of Helicopter Brownout," Proceedings of the 66th Annual American Helicopter Society Forum, Phoenix, AZ, May 11–14, 2010.
- ⁸Wenren, Y., Walter, J., Fan, M., and Steinhoff, J., "Vorticity Confinement and Advanced Rendering to Compute and Visualize Complex Flows, Paper AIAA-2006-945, 44th AIAA Aerospace Sciences Meeting and Exhibit, Reno, Nevada, January 9–12, 2006.
- ⁹Greeley, R., Balme, M. R., Iversen J. D., Metzger, S., Mickelson, R., Phoreman, J., and White, B., "Martian Dust Devils: Laboratory Simulations of Particle Threshold, *Journal of Geophysical Research*, Vol. 108, (E5), 2003.
- ¹⁰Kalra, T. S., Lakshminarayan, V. K, and Baeder, J. D., "CFD Validation of Micro Hovering rotor in Ground Effect," Proceedings of the 66th Annual American Helicopter Society Forum, Phoenix, AZ, May 11–14, 2010.
- ¹¹Lakshminarayan, V. K., "Computational Investigation of Micro-Scale Coaxial Rotor Aerodynamics in Hover," Ph.D. Dissertation, Department of Aerospace Engineering, University of Maryland, College Park, 2009.
- ¹²Buelow P. E. O., Schwer D. A., Feng J., and Merkle C. L., "A Preconditioned Dual-Time, Diagonalized ADI scheme for Unsteady Computations," AIAA paper 1997-2101, 13th AIAA Computational Fluid Dynamics Conference, Snowmass Village, CO, June 29–July 2, 1997.
- ¹³Pandya, S. A., Venkateswaran, S., and Pulliam, T. H. "Implementation of Preconditioned Dual-Time Procedures in OVERFLOW," AIAA paper 2003-0072, 41st AIAA Aerospace Sciences Meeting and Exhibit, Reno, NV, January 6–9, 2003.
- ¹⁴Pulliam, T., and Chaussee, D., "A Diagonal Form of an Implicit Approximate Factorization Algorithm," *Journal of Computational Physics*, Vol. 39, (2), February 1981, pp. 347–363.
- ¹⁵Turkel, E., "Preconditioning Techniques in Computational Fluid Dynamics," *Annual Review of Fluid Mechanics*, Vol. 31, January 1999, pp. 385–416.
- ¹⁶van Leer, B., "Towards the Ultimate Conservative Difference Scheme V. A Second-Order Sequel To Godunov's Method," *Journal of Computational Physics*, Vol. 32, (1), July 1979, pp. 101–136.
- ¹⁷Koren, B., "Multigrid and Defect Correction for the Steady Navier-Stokes Equations," *Journal of Computational Physics*, Vol. 87, (1), March 1990, pp. 25–46.
- ¹⁸Roe, P., "Approximate Riemann Solvers, Parameter Vectors and Difference Schemes," *Journal of Computational Physics*, Vol. 43, (2), October 1981, pp. 357–372.
- ¹⁹Spalart, P. R., and Allmaras, S. R., "A One-equation Turbulence Model for Aerodynamic Flows," AIAA Paper 1992-0439, 30th AIAA Aerospace Sciences Meeting and Exhibit, Reno, NV, January 6–9, 1992.
- ²⁰Duraisamy, K., "Studies in Tip Vortex Formation, Evolution and Control," Ph.D. Dissertation, Department of Aerospace Engineering, University of Maryland, College Park, 2005.
- ²¹Lee, Y., "On Overset Grids Connectivity and Automated Vortex Tracking in Rotorcraft CFD," Ph.D. Dissertation, Department of Aerospace Engineering, University of Maryland, College Park, 2008.
- ²²Bagnold, R., "The Physics of Blown Sand and Desert Dunes," Dover Publications Inc., 1941.
- ²³Lu, H., and Shao, Y., "A New Model for Dust Emission by Saltation Bombardment," *Journal of Geophysical Research*, Vol. 104, (D14), 1999, pp. 16827–16842.
- ²⁴Jeong, J., and Hussain, F., "On the Identification of a Vortex," *Journal of Fluid Mechanics*, Vol. 285, 1995, pp. 69–94.